ROYAL SOCIETY
OF CHEMISTRY

## PAPER

Check for updates

# High temperature (nano)thermometers based on LiLuF$_4$:Er$^{3+}$,Yb$^{3+}$ nano- and microcrystals. Confounded results for core−shell nanocrystals†

Anna M. Kaczmarek, [iD] *[a] Markus Suta,[b] Hannes Rijckaert, [iD] [c]
Thomas P. van Swieten,[b] Isabel Van Driessche,[c] Mariusz K. Kaczmarek[d] and
Andries Meijerink*[b]

Recent technological developments require knowledge of temperature down to the micro- or even nano-scale. Lanthanide-doped nanoparticles became a popular tool to achieve this. Their temperature sensitive luminescence enables their application as remote thermometers and for mapping temperature profiles with high spatial resolution. Applicability of luminescence thermometry is, however, often limited at high temperatures. In nanoelectronics or chemical reactors, high temperatures above 500 K are common and new approaches for accurate high temperature sensing need to be developed. In this work, we report three different shapes of upconverting LiLuF$_4$:2% Er$^{3+}$,18% Yb$^{3+}$ nanocrystals both with and without shells and study the influence of the shell on the thermometric properties. We observed peculiar behavior of the core−shell particles suggesting the presence of the dopants within the protective and 'undoped' shells. Coating the nanoparticles with a silica layer extends the operational temperature range. In an upconversion (UC) Yb$^{3+}$−Er$^{3+}$ system temperature sensing relies on thermal coupling between the $^4S_{3/2}$ and $^2H_{11/2}$ energy levels. At sufficiently high temperatures (>550 K), we observe additional thermal coupling involving the higher $^4F_{7/2}$ energy levels. The larger energy gap allows to increase the relative sensitivity at elevated temperatures and to sustain a high temperature precision over a wider temperature range than for a two-level Boltzmann thermometer. The thermal coupling between the $^4S_{3/2}$ and $^2H_{11/2}$ energy levels is used for lower temperature sensing (<550 K) and the $^4F_{7/2}$ energy level is crucial for higher temperature sensing (>550 K).

## 1. Introduction

Precise (and also accurate) measurement of temperature has become very important in scientific research and development and in technological applications relying on feedback from sensors.[1–4] Many recent developments in technologies urged for reliable thermometers with high spatial resolution, even down to the nanoscale. This involves many fields of applications such as *e.g.* nanoelectronics, nanophotonics, thermal barrier coatings, and chemical (micro) reactors.[5] A representative example are temperature inhomogeneities in chemical reactors that can lead to large variations in activity and selectivity of catalytic reactions.[6,7] Mapping of temperature variations, even down to the single catalyst particle scale, is the first step towards a realization and control of more homogeneous temperature profiles. Also, in the electronic industry, heat dissipation is a limiting factor in the design, miniaturization and functioning of (high power) devices.[8] Traditional macroscopic thermometers are not suitable for temperature sensing in this size regime due to their limited spatial resolution. More importantly, they require physical contact between the sensing element and the temperature-registration instrument. Various optical methods, such as thermography, Raman scattering, thermal reflection and luminescence have been proposed as a basis for alternative remote thermometers.[3,9] Among the different temperature measurement concepts, luminescence-based thermometry is consistently proving to be a very promising alternative, since it only requires the acquisition of an emission spectrum to measure the temperature.[10]

[a] *NanoSensing Group, Department of Chemistry, Ghent University, Krijgslaan 281-S3, B-9000 Ghent, Belgium. E-mail: anna.kaczmarek@ugent.be, a.meijerink@uu.nl*

[b] *Debye Institute for Nanomaterials Science, Utrecht University, Princetonplein 1, 3584 CC Utrecht, The Netherlands*

[c] *SCRIPTs, Department of Chemistry, Ghent University, Krijgslaan 281-S3 B-9000 Ghent, Belgium*

[d] *Department of Mechatronics, Kazimierz Wielki University in Bydgoszcz, Kopernika 1, 85-074 Bydgoszcz, Poland*

† Electronic supplementary information (ESI) available. See DOI: 10.1039/d0tc05865c

Lanthanide-doped inorganic nanoparticles are an interesting class of luminescent thermometers.[11–16] They are especially suitable for high-temperature applications due to the limited thermal quenching at higher temperatures. In addition, their relatively high quantum yields and characteristic line emission at well-defined wavelengths are necessary features for the development of a successful high temperature thermometer.[17,18] The respective emission of different $Ln^{3+}$ ions covers the entire electromagnetic spectrum ranging from UV to IR. This flexibility enables a design of thermometers for a variety of temperature ranges and applications.[10] In $Ln^{3+}$ ions, the partially filled 4f orbitals are well shielded from the chemical surrounding by the filled outer 5s and 5p orbitals. The characteristic luminescence arises from electronic transitions between different microstates within the partly filled $4f^n$ shell ($4f^n \rightarrow 4f^n$ transitions). Thermalization between closely separated states within the energy level landscape of a partially $4f^n$ shell can be accurately monitored by means of the intensity ratio of the respective radiative transitions from the two levels and thus, used for temperature sensing.[19]

In this work, $LiLuF_4$ was selected as the host for obtaining thermometers operating in the high-temperature regime after co-doping with $Yb^{3+}$ and $Er^{3+}$ ions. The upconverting lanthanide couple has already been proven to be promising for high temperature thermometry.[7,14] Hosts such as $LiLuF_4$ or $LiYF_4$ are particularly attractive for $Yb^{3+}$–$Er^{3+}$ upconversion due to their low phonon energies (in the range of 500 cm$^{-1}$) and high crystal field strengths based on the small $Lu^{3+}$ sites.[20,21] Tailoring the local crystal field of the lanthanide ions allows enhancing the UC luminescence intensity since the possibility of intra-4f tranistions of activators is significantly influenced by the host symmetry according to the Judd–Ofelt theory.[21] The small $Lu^{3+}$ ions shorten the average bond lengths of O–Ln, which increases the (odd-parity) crystal field terms for the lanthanide ions and thus increase the probablility of electric dipole transitions, which can enhance the intensity of the upconversion emission.

On the other hand, the $LiLuF_4$ matrix has not been as extensively explored as other fluoride hosts *e.g.* β-$NaYF_4$, β-$NaGdF_4$ or $LaF_3$ and may thus be interesting alternative hosts. Additionally, $LiLuF_4$ (nano-/micro-)particles with various shapes and core–shell architectures can be obtained quite easily using the hydrothermal decomposition synthesis from trifluoroacetic acid precursors.[22–25] Even more importantly, $Ln^{3+}$-doped $LiLuF_4$ nanoparticles have shown high absolute upconversion (UC) quantum yields (QY) exceeding 5%.[26] High QYs are necessary for the development of useful thermometers, since not only high absorption, but also high emission intensities are required. $LiLuF_4$ also shows good thermal stability at elevated temperatures.[27] The $LiYF_4$ host matrix has also proven to be very effective for both upconverted luminescence thermometry with $Er^{3+}$ not only for the sake of temperature measurements, but even for the elucidation of other thermodynamic properties such as thermal conductivities along lipid bilayers grown on the surface of the nanocrystals.[28] This has led to an increasing interest in the $LiLuF_4$ matrix for upconversion

systems and our choice to employ it for high temperature thermometry.

Four materials were prepared in the study – three types of $LiLuF_4$ nanoparticles with different shapes (spherical, cubic and diamond) and micro-sized $LiLuF_4$. Up to date, little is known about the influence of the nanosize and the shape of particles on the thermometry performance. For the preparation of the $LiLuF_4$ nanoparticles two synthesis routes were selected – the co-precipitation route (spheres) and the thermal decomposition route of trifluoroacetate precursors (cubes and diamonds). We aimed at studying the influence of the shape and synthesis route of the nanoparticles on the performance as a luminescent thermometer. Additionally, it was our purpose to elucidate the impact of shells (both undoped $LiLuF_4$ as well as silica) on the properties of $LiLuF_4$ nanoparticles as a thermometer and extend the temperature sensing range towards higher temperatures.

## 2. Experimental section

### 2.1. Synthesis

**General.** $Ln(CF_3COO)_3$ (Ln = Gd, Er, Yb) and $CF_3COOLi$ precursors were prepared according to a previously reported protocol.[21] All other chemicals were commercially purchased and used without further purification.

**Synthesis of spherical $LiLuF_4$ nanocrystals (core nanocrystals).** The spherical $LiLuF_4$ nanocrystals were synthesized according to a previously reported protocol.[21] In a typical synthesis, 0.25 mmol of LiCl, 0.145 mmol of $LuCl_3·6H_2O$, 0.005 mmol $ErCl_3·6H_2O$ and 0.1 mmol $YbCl_3·6H_2O$ were mixed with 4 mL of oleic acid and 6 mL of 1-octadecene in a 50 mL three-necked round-bottom flask. The mixture was heated to 120 °C under vacuum for 30 min with constant stirring. Subsequently, it was heated to 160 °C under $N_2$ flow and constant stirring for 30 min until a clear solution formed. Afterwards, it was cooled down to room temperature. Next, 2.5 mL of methanol (MeOH) solution containing 1 mmol of $NH_4F$ was quickly added and the solution stirred at 50 °C for 30 min to allow nanocrystal growth. After evaporation of the excess MeOH, the resulting solution was heated to 300 °C under $N_2$ flow and vigorous stirring for 60 min. The obtained $LiLuF_4$ nanocrystals were precipitated by adding a large volume of acetone and isolated by centrifugation. They were washed three times with acetone, and finally redispersed in cyclohexane.

**Synthesis of cubic $LiLuF_4$ nanocrystals (core nanocrystals).** The cubic $LiLuF_4$ nanoparticles were synthesized according to a previous report protocol.[26] In a typical synthesis, 1 mmol of $CF_3COOLi$, 0.80 mmol of $Lu(CF_3COO)_3$, 0.18 mmol $Yb(CF_3COO)_3$ and 0.02 mmol $Er(CF_3COO)_3$ were mixed with 6 mL of oleic acid, 2 mL of 1-octadecene and 2 mL of oleylamine in a 50 mL three-necked round-bottom flask. The mixture was heated to 120 °C under vacuum for 30 min under constant stirring. Afterwards, the mixture was kept at that temperature under $N_2$ flow and constant stirring for additional 30 min until a clear yellow solution formed. Next, the solution was heated to 320 °C

**3590** | *J. Mater. Chem. C*, 2021, **9**, 3589–3600

This journal is © The Royal Society of Chemistry 2021

under $N_2$ flow and vigorous stirring for 40 min. The obtained core $LiLuF_4$ cubic nanocrystals were precipitated by addition of a large volume of acetone and isolated by centrifugation. They were washed three times with acetone, and finally redispersed in cyclohexane.

**Synthesis of core–shell cubic $LiLuF_4$:Er,Yb@$LiLuF_4$ nanocrystals.** The cubic core–shell $LiLuF_4$ nanocrystals were synthesized according to a previously reported protocol.[26] For the preparation of the core solution, 1 mmol of $CF_3COOLi$ and 1 mmol of $Lu(CF_3COO)_3$ were mixed with 9 mL of oleic acid, 2 mL of 1-octadecene and 9 mL of oleylamine in a 50 mL three-necked round-bottom flask. The mixture was heated to 120 °C under vacuum for 30 min under constant stirring, and kept at 120 °C under $N_2$ flow and constant stirring for additional 30 min until a clear yellow solution formed. Afterwards, the solution was cooled down to room temperature. Next, the core nanocrystals were prepared according to above procedure. After 40 min of heating at 320 °C under $N_2$ flow, the first batch of a solution containing the shelling agents was slowly injected (2 mL). The resulting mixture was heated for 10 min at 320 °C under $N_2$ flow. Following this procedure, three or six shells were grown around the core nanocrystals. The obtained core–shell $LiLuF_4$ cubic nanocrystals were precipitated by addition of a large volume of acetone and isolated by centrifugation. They were washed three times with acetone, and finally redispersed in cyclohexane.

**Synthesis of core–shell cubic $LiLuF_4$:Er,Yb@$LiLuF_4$ nanocrystals coated with $SiO_2$.** The core–shell cubic $LiLuF_4$ nanocrystals were prepared according to the previously described procedure. The thus obtained nanocrystals were coated with a $SiO_2$ shell by means of a reverse microemulsion method. First, 32 mg of the nanocrystals were dispersed in 10 mL of cyclohexane and 0.4 g of IGEPAL CO-520 was added. After stirring of the solution for 10 min, 1.6 g of IGEPAL CO-520 was added. Afterwards, 80 μL of $NH_4OH$ (28–30%) was added to form a water-in-oil microemulsion. The solution was sonicated for 30 min. Next, 40 μL of TEOS (tetraethyl orthosilicate) was added and the resulting solution stirred at 300 RPM for 48 h. The particles were precipitated by addition of acetone and collected by centrifugation. The particles were washed two times with water and one more time with ethanol (EtOH) and finally redispersed in water.

**Synthesis of diamond-shaped $LiLuF_4$ nanocrystals (core nanocrystals).** The diamond-shaped $LiLuF_4$ nanocrystals were synthesized according to a previously reported protocol with modifications.[26] In a typical synthesis, 1 mmol of $CF_3COOLi$, 0.80 mmol of $Lu(CF_3COO)_3$, 0.18 mmol $Yb(CF_3COO)_3$ and 0.02 mmol $Er(CF_3COO)_3$ were mixed with 4 mL of oleic acid and 6 mL of 1-octadecene in a 50 mL three-necked round-bottom flask. The mixture was heated to 120 °C under vacuum for 30 min and constant stirring. Afterwards, it was kept at 120 °C under $N_2$ flow and constant stirring for 30 min until a clear yellow solution formed. Next, the solution was heated to 320 °C under $N_2$ flow and vigorous stirring for 40 min. The obtained core $LiLuF_4$ diamond-shaped nanocrystals were precipitated by addition of a large volume of acetone and

collected by centrifugation. They were washed three times with acetone, and finally re-dispersed in cyclohexane.

**Synthesis of core–shell diamond-shaped $LiLuF_4$:Er,Yb@ $LiLuF_4$ nanocrystals.** The diamond-shaped core–shell $LiLuF_4$ nanocrystals were synthesized according to a previously reported protocol.[26] For the preparation of the core solution, 1 mmol of $CF_3COOLi$ and 1 mmol of $Lu(CF_3COO)_3$ were mixed with 9 mL of oleic acid, 2 mL of 1-octadecene and 9 mL of oleylamine in a 50 mL three-necked round-bottom flask. The mixture was heated to 120 °C under vacuum for 30 min and constant stirring, and subsequently kept at that temperature under $N_2$ flow and constant stirring for additional 30 min until a clear yellow solution formed. The solution was next cooled down to RT. Next the core nanocrystals were prepared according to the previously described procedure. After 40 min of heating at 320 °C under $N_2$ flow, the first batch of a solution containing the shelling agents was slowly injected (2 mL). It was heated for additional 10 min at 320 °C under $N_2$ flow. Following this procedure three or six shells were grown around the nanocrystals. The thus obtained core–shell $LiLuF_4$ nanocrystals were precipitated by addition of a large volume of acetone and isolated by centrifugation. They were washed three times with acetone, and finally re-dispersed in cyclohexane.

**Synthesis of microcrystalline $LiLuF_4$.** Microcrystalline $LiLuF_4$ was synthesized. First, 1 mL of a $Lu(NO_3)_3 \cdot 6H_2O$ (0.5 M), 0.18 mL of a $Yb(NO_3)_3 \cdot 6H_2O$ (0.5 M), and 0.02 mL of an $Er(NO_3)_3 \cdot 6H_2O$ (0.5 M) solution were mixed, respectively, and the resulting solution stirred. Next, 6.0 mL $NH_4F$ (0.5 M) and 4.0 mL LiF (0.5 M) was added to the solution. The mixture was stirred for 30 min until a colorless precipitate settled. The suspension was placed in an oven, set at 100 °C, to evaporate excess solvent and the remaining powder heat treated at 300 °C. The obtained solid was washed two times with deionized water and two times with EtOH to remove any unreacted starting materials.

## 2.2. Characterization

**(Time-resolved) luminescence spectroscopy and thermometry.** Luminescence spectra were measured on an Edinburgh FLS920 spectrofluorometer equipped with a Hamamatsu R928P photomultiplier tube (PMT, Hamamatsu, Shizuoka, Japan) used to detect the emission signals in the near UV to visible range. All emission spectra were acquired by excitation with continuous wave (CW) power-tunable (power limit: $P_{max}$ = 2 W, Livingston, UK) laser operating at $\lambda_{ex}$ = 980 nm. Luminescence decay curves in the microsecond domain were obtained by excitation with a pulsed wavelength-tunable (Carlsbad, CA, USA) Opotek Opolette 355 LD optical parametric oscillator (OPO) with a repetition rate of 20 Hz and temporal pulse width of around 6 ns. The time-dependent signal was processed in a multichannel scaler (MCS). Temperature-dependent emission spectra above room temperature of the powders were measured in a Linkam (Surrey, UK) THMS600 Microscope Stage ($\pm$ 0.1 °C temperature stability) that could be placed in the spectrometer. For all measurements the same amount of powder was placed in the Linkam Stage. Low temperature measurements were performed using an ARS (Advanced Research Systems, USA)

This journal is © The Royal Society of Chemistry 2021

*J. Mater. Chem. C*, 2021, **9**, 3589–3600 | **3591**

closed cycle cryostat coupled with an Edinburgh Instruments FLSP920 UV-vis-NIR spectrometer setup. Here, a Hamamatsu R928P photomultiplier tube (PMT, Hamamatsu, Shizuoka, Japan) was used to detect the emission signals. The corresponding emission spectra were also acquired by excitation with CW (power limit: $P_{max}$ = 800 mW, Livingston, UK) laser operating at $\lambda_{ex}$ = 980 nm. All emission spectra in the manuscript have been corrected for the collection efficiency of luminescence. All the temperature-dependent data was processed employing the TeSen software: http://www.tesen.ugent.be.

**TEM, SEM, powder X-ray diffraction.** Transmission electron microscope (TEM) images were acquired on a JEOL JEM-2200FS TEM operated at 200 kV and equipped with $C_s$ corrector. The samples were prepared by dipping a 300-mesh holey carbon copper grid into the purified nanoparticle suspensions. Scanning TEM (STEM) images were taken with high-angle annular dark field (HAADF) detector. The composition of the sample was determined *via* energy dispersive X-ray (EDX) spectroscopy in HAADF-STEM mode.

Scanning electron microscopy (SEM) measurements were performed using a FEI Quanta 200 FSEM and a FEI Nova 600 Nanolab Dual-Beam focused ion beam in secondary electron mode. Powder XRD patterns were recorded by a Thermo Scientific ARL X'TRA diffractometer equipped with a Cu Kα1 ($\lambda$ = 1.5405 Å) source, a goniometer and a Peltier-cooled Si (Li) solid-state detector.

## 3. Results and discussion

LiLuF$_4$ crystallizes in a scheelite structure (space group $I4_1/a$, no. 88), in which the Lu$^{3+}$ ions are surrounded by eight F$^-$ ions that form the edges of a slightly distorted square antiprism.[25] There is no scheelite single crystal structure of LiLuF$_4$ deposited in the ICSD database, however, both LiYF$_4$ and LiLuF$_4$ crystalize isotopically.[29] Alternatively, a single crystal structure of the monoclinic fergusonite LiLuF$_4$ ($C12/c1$) is known, which is obtained under elevated pressures.[30] From solution, however, it is expected that the thermodynamically more stable scheelite phase precipitates at ambient pressure. In the scheelite-type LiLuF$_4$ crystal structure all Lu$^{3+}$ ions occupy a single crystallographic $4b$ site with local $S_4$ symmetry. LiLuF$_4$:2% Er$^{3+}$,18% Yb$^{3+}$ nanocrystals with spherical, cubic and diamond habitus were prepared using either the co-precipitation method (spheres) or thermal decomposition of trifluoroacetic acid precursors (cubes and diamonds). These nanocrystals were synthesized with oleic acid and other hydrophobic ligands (oleylamine) as surfactant, which enabled dispersion in cyclohexane as well as other nonpolar organic solvents to form stable colloidal suspensions. The nanocrystals were characterized by powder X-ray diffraction (PXRD, Fig. 1). Additionally, for comparative purposes, micro-sized LiLuF$_4$:2% Er$^{3+}$,18% Yb$^{3+}$ was also prepared using a hydrothermal synthesis and characterized together with the nanocrystals. The nanocrystals as well as microsized LiLuF$_4$:2% Er$^{3+}$,18%
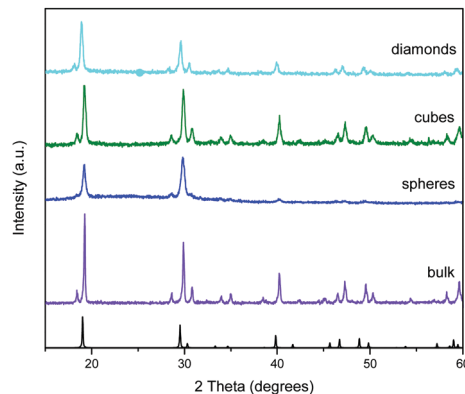


**Fig. 1** Powder XRD patterns of bulk LiLuF$_4$:2% Er$^{3+}$,18% Yb$^{3+}$ (purple line), LiLuF$_4$:2% Er$^{3+}$,18% Yb$^{3+}$ spheroidal nanocrystals (dark blue line), LiLuF$_4$:2% Er$^{3+}$,18% Yb$^{3+}$ cuboidal nanoparticles (cyan line), and LiLuF$_4$:2% Er$^{3+}$,18% Yb$^{3+}$ diamond-shaped nanocrystals (light blue line).

Yb$^{3+}$ could be well indexed to the tetragonal LiLuF$_4$ (JCPDS No. 027-1251) with some additional reflections at $2\theta$ = 18.5° and 28.7° observed in the powder patterns.[25,26] These additional reflections cannot be assigned to the starting materials or LuF$_3$. The PXRD patterns indicate that the spheroidal particles have lowest crystallinity, which is linked to the lower synthesis temperature compared to the cubes and diamonds. Transmission electron microscopy (TEM) images (Fig. 2) show that the three types of morphology of the LiLuF$_4$ nanoparticles can be obtained by careful control of the synthesis conditions. The co-precipitation synthesis at 300 °C with chloride salts and NH$_4$F as the starting materials affords spheroidal LiLuF$_4$ nanoparticles with an average size of 30–40 nm (Fig. 2a and b) and weakly defined crystal facets. This leads to the dominance of only a few Bragg reflections in the PXRD (Fig. 1). Usage of the thermal decomposition synthesis with trifluoroacetic acid precursors and variation of the type and amount of surfactant ligands yields either cubic or diamond-shaped LiLuF$_4$ nanocrystals (Fig. 2c–f). The cubes had an average size of 20–25 nm, while the diamonds had sizes of around 30 nm
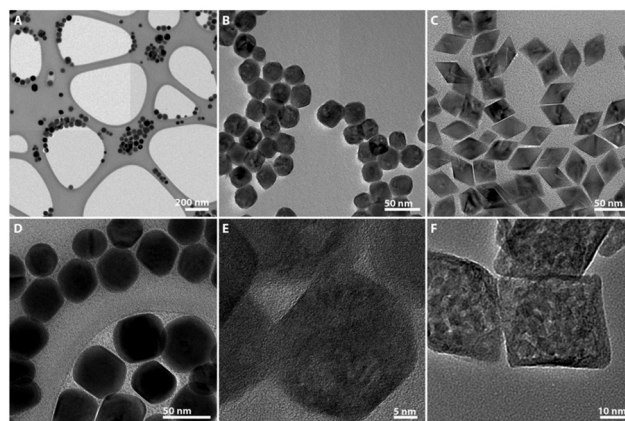


**Fig. 2** TEM images of: (A) and (D) LiLuF$_4$:2% Er$^{3+}$,18% Yb$^{3+}$ spheroidal nanocrystals, (B) and (E) LiLuF$_4$:2% Er$^{3+}$,18% Yb$^{3+}$ cuboidal nanocrystals, and (C) and (F) LiLuF$_4$:2% Er$^{3+}$,18% Yb$^{3+}$ diamond-shaped nanocrystals shown at different magnifications.
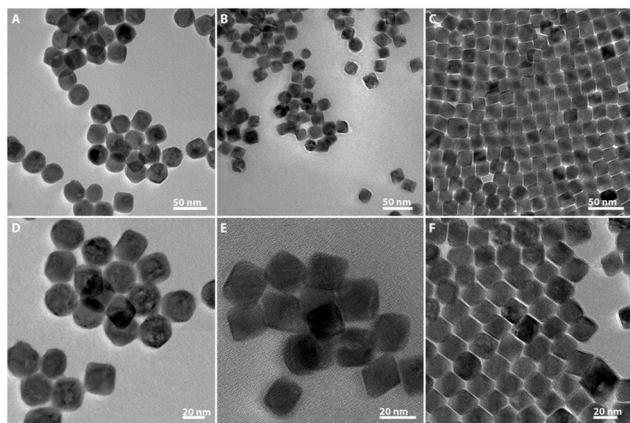
Fig. 3 TEM images of: (A) and (D) LiLuF$_4$:2% Er$^{3+}$,18% Yb$^{3+}$ core-only cuboidal nanocrystals, (B) and (E) LiLuF$_4$:2% Er$^{3+}$,18% Yb$^{3+}$@LiLuF$_4$ core–shell cuboidal nanocrystals (three shells), and (C) and (F) LiLuF$_4$:2% Er$^{3+}$,18% Yb$^{3+}$@LiLuF$_4$ core–shell cuboidal nanocrystals (six shells) shown at different magnifications.
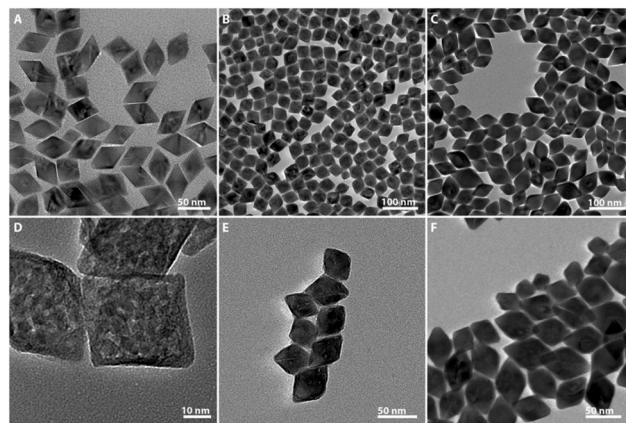


Fig. 4 TEM images of: (A) and (D) LiLuF$_4$:2% Er$^{3+}$,18% Yb$^{3+}$ core only diamond-shaped nanocrystals, (B) and (E) LiLuF$_4$:2% Er$^{3+}$,18% Yb$^{3+}$@LiLuF$_4$ core–shell diamond-shaped nanocrystals (three shells), and (C) and (F) LiLuF$_4$:2% Er$^{3+}$,18% Yb$^{3+}$@LiLuF$_4$ core–shell diamond-shaped nano-crystals (six shells) shown at different magnifications.

along the longest axes. Both types of particles show good size dispersion based on TEM analysis. As the spherical LiLuF$_4$ nanoparticles showed lowest degree of crystallinity, which, as will be shown later in the paper, adversely affected the luminescence intensity of the material, they were not selected for coating with an inert shell. Additionally, it should be mentioned that control of the size and shape of uniform particles is much more difficult in the co-precipitation synthesis method. For these reasons, it was discarded from further experiments involving modifications of the particles. Three and six shells were grown around the cubes and diamonds yielding nanocrystals with the same morphology but showing a systematic increase in size with the number of shells grown around them. Growth of six shells around the cubes increased the average size of the nanocrystals to around 25–30 nm (Fig. 3), while the size of the diamondals increased to around 50–55 nm along the longer axes and around 30 – 35 nm for the shorter axes (Fig. 4). Also in the case of the diamond-shaped particles we see larger size dispersion than in the case of the cubes. In the case of the cube nanoparticles, shelling of the nanocrystals induced a diamond shape for some of the nanocrystals, which is a consequence of the anisotropic space group that LiLuF$_4$ crystallizes in. Overall, both PXRD and TEM revealed that LiLuF$_4$ nanocrystals with different shapes, sizes, and additional layers of shells could be synthesized.

In order to investigate the suitability of these materials for luminescence thermometry over a wide temperature range, emission spectra of the compounds were recorded at varying temperatures. Fig. S1a (ESI†) shows the UC emission spectra recorded between 303 and 523 K (with intervals of 22 K) upon excitation of Yb$^{3+}$ at 980 nm using a continuous wave (CW) laser. The peaks with maximum at 525 nm are assigned to $^2$H$_{11/2}$ → $^4$I$_{15/2}$ transitions (500–532 nm) and the peaks with maximum at 550 nm to $^4$S$_{3/2}$ → $^4$I$_{15/2}$ transitions (532–570 nm) (Fig. S1a, ESI†). Yb$^{3+}$–Er$^{3+}$ upconversion based thermometry relies on the ratio of the integrated emission intensities (or peak maxima) from the thermally coupled excited states $^2$H$_{11/2}$ and $^4$S$_{3/2}$.[31]

It should be mentioned here that from the theoretical point for view intensity ratio calculations carried out based on the integrated intensities are more reliable. However, in the case of the investigated materials, at higher temperatures, the spectral overlap between the $^2$H$_{11/2}$ → $^4$I$_{15/2}$ and $^4$S$_{3/2}$ → $^4$I$_{15/2}$ related emission bands pose a systematic error in the intensity ratio ($\Delta$ parameter) calculations. Therefore, although considering peak maxima for calculations is less reliable due to differences in intensity distribution over the peaks, this approach was also considered here for comparison.

The population ratio of two thermally coupled excited states is determined by the Boltzmann distribution. The thermometric parameter $\Delta$ being the intensity ratio of the two previously mentioned radiative transitions is an important parameter for evaluating the performance of optical thermometers and obeys (eqn (1)).

$$\Delta_1 = \alpha \exp\left(-\frac{\Delta E}{k_B T}\right) \qquad (1)$$

where the pre-factor $\alpha = Cg_2/g_1$. $C$ contains information about the ratio of the radiative transition probabilities from the two thermally coupled levels to the addressed ground level, while $g_2$ and $g_1$ are the $(2J + 1)$-fold degeneracies of the thermally coupled levels, and $\Delta E$ is the effective energy gap between the two excited levels.[32] The experimentally determined intensity ratios between luminescence from the $^2$H$_{11/2}$ and $^4$S$_{3/2}$ levels, respectively, were fitted to the model of eqn (1) to obtain $\Delta E = (720 \pm 38)$ cm$^{-1}$ ($R^2 = 0.992$), which is close to the values found in literature for this energy gap around 800 cm$^{-1}$ (Fig. S1c, ESI†), e.g. in LaF$_3$.[33] Using the fitted energy gap, we express the performance of this thermometer in terms of the relative sensitivity $S_r$ (eqn (2)). It indicates the relative change of the thermometric parameter per unit temperature (in % K$^{-1}$) and is independent of the operational principle of the thermometer. It thus allows a direct and quantitative comparison of different

This journal is © The Royal Society of Chemistry 2021

J. Mater. Chem. C, 2021, 9, 3589–3600 | 3593

thermometers.[34]

$$S_r = 100\% \times \left| \frac{1}{\Delta} \frac{\partial \Delta}{\partial T} \right| = 100\% \times \frac{\Delta E}{k_B T^2} \qquad (2)$$

The maximum relative sensitivity for the spherical LiLuF$_4$:2% Er$^{3+}$,18% Yb$^{3+}$ nanoparticles was calculated to be 1.12%K$^{-1}$ at 303 K (Fig. S1d, ESI†). However, it is the temperature uncertainty ($\delta T$) that is the most important parameter to assess the performance of a thermometer, since it not only includes the relative sensitivity but also the error on the intensity ratio ($\delta \Delta$).[35]

$$\delta T = \frac{1}{S_r} \frac{\delta \Delta}{\Delta} \qquad (3)$$

A statistically expected temperature uncertainty $\delta T < 2.5$ K was determined for the spherical nanoparticles throughout the whole studied temperature range (Fig. S1e, ESI†). While the relative sensitivity is predominantly governed by the energy gap between the two thermally coupled levels of interest, a low temperature uncertainty is obtained by selection of those nanoparticles that show stronger emission intensity. A poor crystallinity reduces the upconversion emission intensity of the Er$^{3+}$ ions, which is thus counterproductive for a low temperature uncertainty. Fig. 5 depicts the emission spectra recorded between 303 and 523 K upon excitation of Yb$^{3+}$ at 980 nm of the cubic LiLuF$_4$:2% Er$^{3+}$,18% Yb$^{3+}$ nanoparticles – core only (Fig. 5a), with three shells (Fig. 5b) and six shells (Fig. 5c) of undoped LiLuF$_4$, respectively. The temperature-dependent integrated areas under the respective emission peaks for the different nanoparticles are depicted in Fig. 5d–f (blue circles are shown for 525 nm peaks, black squares for the 550 nm peaks). We observe that in the core-only LiLuF$_4$:2% Er$^{3+}$,18% Yb$^{3+}$ nanocrystals, the intensity of the $^2H_{11/2} \rightarrow {}^4I_{15/2}$-related emission (525 nm) increases whereas the intensity of $^4S_{3/2} \rightarrow {}^4I_{15/2}$-(550 nm) peaks decrease with an increase in temperature. However, with the successive growth of inert LiLuF$_4$ shells, this behavior changes. If the LiLuF$_4$:2% Er$^{3+}$,18% Yb$^{3+}$ nanocrystals are coated with six undoped LiLuF$_4$ shells, we observe that both the intensities of the emission peaks at 525 nm and 550 nm

increase with increasing temperature, respectively. These observations will be discussed in more detail below.

We investigated the thermometric properties of the core and core–shell (with 3 or 6 shells) LiLuF$_4$:2% Er$^{3+}$,18% Yb$^{3+}$ nanoparticles. The $\Delta$ parameter, relative sensitivity and temperature uncertainty have been determined and the graphs are presented in Fig. 6. In Table 1 these values are presented for the cubic nanoparticles. No significant differences in the $S_r$ value are observed in the core–shell systems compared to the core-only nanoparticles, since the energy difference $\Delta E$ between the $^4S_{3/2}$ and $^2H_{11/2}$ level is similar for the different systems. However, it is clear that for the core–shell systems a lower temperature uncertainty can be obtained. This observation is a consequence of the higher emission intensity in the shelled nanocrystals (after growing six shells around the cubic nanocrystals the emission intensity rises almost one order of magnitude).

The thermometric performance of the diamond-shaped LiLuF$_4$:2% Er$^{3+}$,18% Yb$^{3+}$ nanocrystals at elevated temperatures (303–523 K) has also been studied for core-only as well as core–shell nanoparticles with three or six undoped LiLuF$_4$ shells. The results are presented in the ESI† (Fig. S2 and S3). The diamond-shaped nanocrystals showed an increase in the emission intensity at elevated temperatures, which is a similar trend to that observed for the cubic nanocrystals. Likewise, the diamond-shaped nanocrystals also showed very promising thermometric performance, although the higher emission intensity of the cubic nanocrystals afforded slightly lower temperature uncertainties than the cubic nanocrystals. The exact thermometric
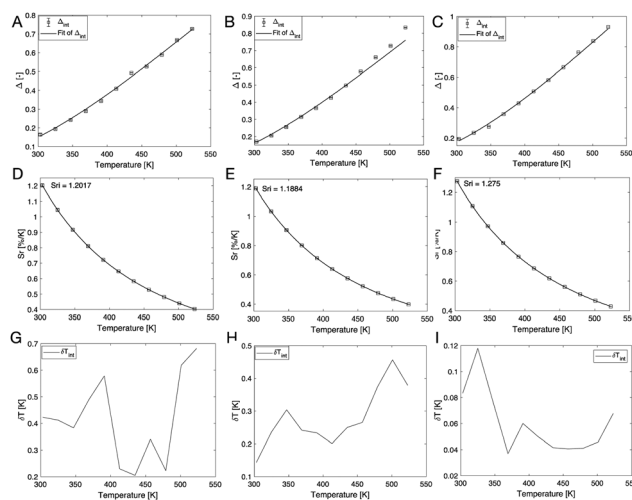


**Fig. 6** (A), (D) and (G) LiLuF$_4$:2% Er$^{3+}$,18% Yb$^{3+}$ core-only cubic nanocrystals, (B), (E) and (H) LiLuF$_4$:2% Er$^{3+}$,18% Yb$^{3+}$@LiLuF$_4$ core–shell cubic nanocrystals (three shells), (C), (F) and (I) LiLuF$_4$:2% Er$^{3+}$,18% Yb$^{3+}$@LiLuF$_4$ core–shell cubic nanocrystals (six shells). Top: Plots showing the calibration curves for the core-only and core–shell LiLuF$_4$:2% Er$^{3+}$,18% Yb$^{3+}$ cubic nanocrystals upon usage of eqn (1). The points show the experimental delta parameters (see eqn (1)) and the solid line shows the least squares fit to the experimental points. Middle: plots of the relative sensitivity $S_r$ at varying temperatures (303–523 K), the solid lines are a guide for the eyes. Bottom: Graphs depicting the temperature uncertainty over the regarded temperature range. The thermometric parameters for the compounds have been presented in Table 1.
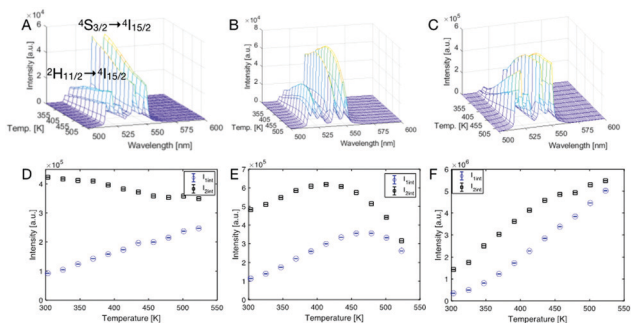


**Fig. 5** Emission spectra and values of integrated intensities as a function of temperature (blue circles are the peaks at 525 nm and black squares are peaks at 550 nm) for: (A) and (D) LiLuF$_4$:2% Er$^{3+}$,18% Yb$^{3+}$ core-only cubic nanocrystals, (B) and (E) LiLuF$_4$:2% Er$^{3+}$,18% Yb$^{3+}$@LiLuF$_4$ core–shell cubic nanocrystals (three shells), and (C) and (F) LiLuF$_4$:2% Er$^{3+}$,18% Yb$^{3+}$@LiLuF$_4$ core–shell cubic nanocrystals (six shells).

**3594** | *J. Mater. Chem. C*, 2021, **9**, 3589–3600

This journal is © The Royal Society of Chemistry 2021

**Table 1** Overview of the thermometric parameters for the LiLuF$_4$:Er$^{3+}$,Yb$^{3+}$ cubic nanocrystals

| Compound | Cubic LiLuF$_4$:Er,Yb | Cubic LiLuF$_4$:Er,Yb@LiLuF$_4$ (three shells) | Cubic LiLuF$_4$:Er,Yb@LiLuF$_4$ (six shells) |
|---|---|---|---|
| $\Delta E$ | $(767 \pm 23)$ cm$^{-1}$ | $(758 \pm 63)$ cm$^{-1}$ | $(813 \pm 19)$ cm$^{-1}$ |
| $R^2$ | 0.997 | 0.983 | 0.998 |
| $S_r$ | 1.2017% K$^{-1}$ (303 K) | 1.1884% K$^{-1}$ (303 K) | 1.2753% K$^{-1}$ (303 K) |
| $\delta T$ | <0.7 K | <0.46 K | <0.12 K |

parameters of the diamond-shaped nanoparticles are compiled in Table S1 (ESI†). Although based on these results conclusions could be drawn that the particle shape has an influence on the emission intensity, one must keep in mind that different synthesis environments were used, which affect the intensity by variations in surface defects, OH incorporation and crystallinity. It should also instead be kept in mind that the surface-to-volume ratios are not the same for the differently shaped and sized nanocrystals. Moreover, the growth of inorganic shells improved the $\delta T$ values. Previously it has been observed that this can be caused by reduced (surface) quenching for the levels that participate in the upconversion mechanism.[36] This is explored further in the manuscript. It is noteworthy that the nanoparticles were only heated up to 523 K as at higher temperatures the samples became visibly brownish and TEM analysis indicated aggregation of the nanoparticles, most likely as a result of the thermal degradation of the capping ligands (oleic acid, and oleylamine). A representative TEM image of diamond-shaped LiLuF$_4$:2% Er$^{3+}$,18% Yb$^{3+}$ nanocrystals after heating above 523 K is depicted in Fig. S4 (ESI†). It has previously been reported by Geitenbeek *et al.* that growing a silica shell around inorganic nanoparticles can extend the temperature range of thermometry with fluoride nanocrystals above 900 K.[14] We have followed that strategy and have grown a silica shell around the LiLuF$_4$:2% Er$^{3+}$,18% Yb$^{3+}$@LiLuF$_4$ cubic core–shell nanoparticles with six shells as a proof of principle. The silica shell was grown employing a reversed microemulsion method and resulted in an evenly spread silica layer with a thickness of around 10 nm (Fig. 7a and b). In Fig. 7c and d the emission spectra of the LiLuF$_4$:2% Er$^{3+}$,18% Yb$^{3+}$@SiO$_2$ recorded up to 809 K are depicted. Higher temperatures were not explored due to limitations of the equipment. The material still showed high stability at this temperature (no change of the nanomaterial body color) clearly showing the beneficial effect of the SiO$_2$ shell. The intensity of the $^2$H$_{11/2}$ → $^4$I$_{15/2}$ (525 nm), $^4$S$_{3/2}$ → $^4$I$_{15/2}$ (550 nm) and $^4$F$_{9/2}$ → $^4$I$_{15/2}$ (665 nm) emission peaks showed different behavior with increasing temperature. First, an enhancement of the emission intensity was observed for all transition peaks followed by a drop in intensity at higher temperatures (Fig. S5, ESI†). It is not straightforward to separately calculate the integrated intensities of the $^2$H$_{11/2}$ → $^4$I$_{15/2}$ and $^4$S$_{3/2}$ → $^4$I$_{15/2}$ transitions due to spectral overlap around 535 nm (Fig. 7d). Therefore, Gaussian fits for every transition peak were used in order to deconvolute the two radiative transitions. The experimentally derived intensity ratio ($\Delta$) was fitted using eqn (1) (Fig. S6, ESI†). However, both fitting of the ratio based on peak maxima and integrated intensities under the peaks revealed that the
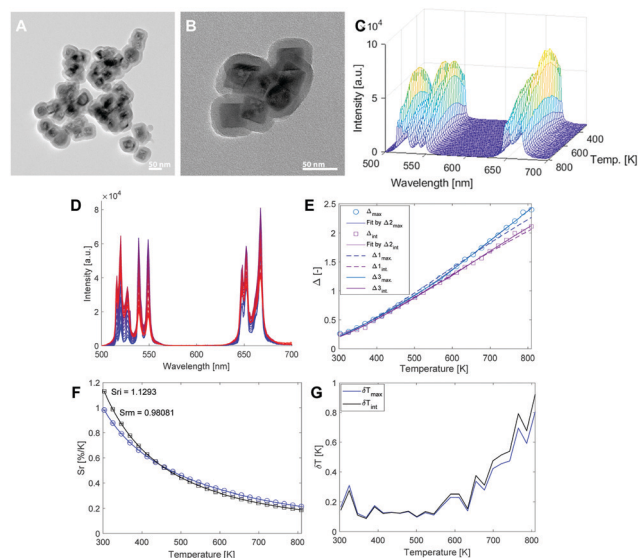


**Fig. 7** (A) and (B) TEM images of LiLuF$_4$:2% Er$^{3+}$,18% Yb$^{3+}$@LiLuF$_4$@SiO$_2$ nanocrystals. (C) and (D) two different visualizations of the emission maps for LiLuF$_4$:2% Er$^{3+}$,18% Yb$^{3+}$@LiLuF$_4$@SiO$_2$ nanocrystals recorded from 303 K to 809 K. In (D), blue colors indicate lower temperatures and red colors higher temperatures. (E) Plot depicting the calibration curves (blue-based on peak maxima, purple-based on integrated area under the peaks) for the LiLuF$_4$:2% Er$^{3+}$,18% Yb$^{3+}$@LiLuF$_4$@SiO$_2$ nanocrystals. The points show the experimental delta parameters and the solid lines the least-squares fits to the experimental points. Upon usage of eqn (1) (dashed lines; $\Delta$1), fit of two separate data ranges to eqn (1) upon separation of the data at 567 K (thin continuous line; $\Delta$2), and upon usage of eqn (4) (thick continuous line; $\Delta$3). The fits for $\Delta$2 and $\Delta$3 overlap. (F) Plot of the relative sensitivity $S_r$ of the measure $\Delta$3 at varying temperatures (303–809 K), calculated for both peak maxima and integrated area under the peaks. The solid line is a guide for the eyes. (G) Graph depicting the temperature uncertainty over the regarded temperature range, calculated both for peak maxima and integrated area under the peaks.

experimental data does not follow a simple Boltzmann distribution (eqn (1)), but shows an onset of a second Boltzmann-like distribution above 555 K. We have attempted fitting the data by dividing it into two parts (303–567 K and 589–809 K; Fig. S7, ESI†) or by using a double Boltzmann distribution (eqn (4)),

$$\Delta_2 = \alpha_1 \exp\left(-\frac{\Delta E_1}{k_B T}\right) + \alpha_2 \exp\left(-\frac{\Delta E_2}{k_B T}\right) \quad (4)$$

A mathematical justification of the latter fitting model is given in the ESI.† It is noteworthy that this type of a double Boltzmann distribution can only be understood from a spectral overlap between emissions from the two thermally excited
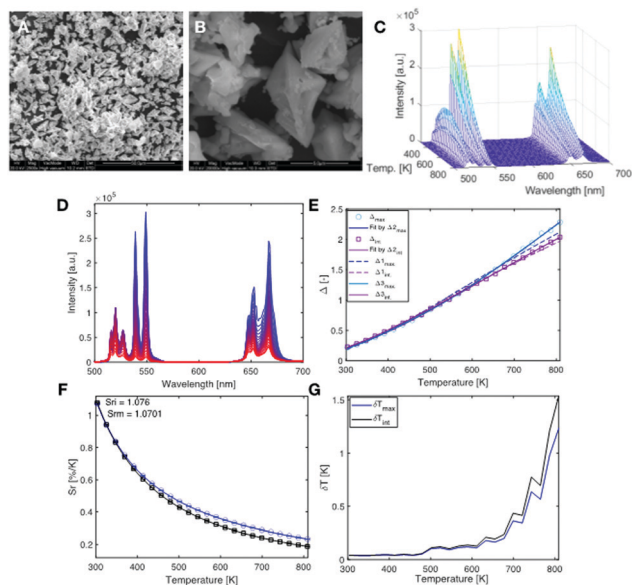
This journal is © The Royal Society of Chemistry 2021

*J. Mater. Chem. C*, 2021, **9**, 3589–3600 | **3595**

Fig. 8   (A) and (B) SEM images of LiLuF$_4$:2% Er$^{3+}$,18% Yb$^{3+}$ microcrystals. (C) and (D) depict two different visualizations of the Er$^{3+}$-based emission maps for LiLuF$_4$:2% Er$^{3+}$,18% Yb$^{3+}$ microcrystals recorded from 303 K to 809 K. In (D) blue colors indicate lower temperatures and red colors higher temperatures. (E) Plot depicting the calibration curves (blue-based on peak maxima, purple-based on the integrated intensity) for the LiLuF$_4$:2% Er$^{3+}$,18% Yb$^{3+}$ microcrystalline particles. The points show the experimental $\Delta$ parameters and the solid line shows the least-squares fit to the experimental points. Usage of eqn (1) (dashed lines; $\Delta 1$), fit of two separate data ranges to eqn (1) upon separation of the data at 567 K (thin continuous line; $\Delta 2$), and upon usage of eqn (4) (thick continuous line; $\Delta 3$). The fits for $\Delta 2$ and $\Delta 3$ overlap. (F) Plot of the relative sensitivity $S_r$ at varying temperatures (303–809 K), calculated for both peak maxima and integrated areas under the peaks. The solid line is a guide for the eyes. (G) Graph depicting the temperature uncertainty over the regarded temperature range, calculated both for peak maxima and integrated area under the peaks.

higher levels. Otherwise, even thermal excitation into a third excited level would not lead to the observation of a biexponential behaviour as suggested by eqn (4). Despite an apparently separate $^4F_{7/2} \rightarrow {}^4I_{15/2}$-based emission Lu$^{3+}$ sites is expected to lead to a large anisotropic crystal field in LiLuF$_4$:Er$^{3+}$, Yb$^{3+}$ at higher temperatures (see Fig. S10, ESI†), the tetragonal crystal system and the related $S_4$ symmetry of the potential. This could split the $^4F_{7/2}$ level into two separate groups of Stark levels in a

similar way as the $^4S_{3/2}$ level (see Fig. S8, ESI†) thus inducing such a (weak) spectral overlap between the $^4F_{7/2} \rightarrow {}^4I_{15/2}$- and $^2H_{11/2} \rightarrow {}^4I_{15/2}$-related emission. It should also be highlighted that employing a biexponential equation for the fitting (compared to separation of the data into two single exponentials) is the more correct approach. We have carried out the same investigation for the micro-sized LiLuF$_4$:2% Er$^{3+}$,18% Yb$^{3+}$ and observed quite similar behavior to that of the LiLuF$_4$:2% Er$^{3+}$,18% Yb$^{3+}$@LiLuF$_4$@SiO$_2$ nanoparticles (Fig. 8). Also in the case of a microcrystalline control sample, a double Boltzmann distribution gave best fits. The fitted parameters obtained by a least-squares fit from the data to eqn (4) for nanocrystalline LiLuF$_4$:2% Er$^{3+}$,18% Yb$^{3+}$@LiLuF$_4$@SiO$_2$ and microcrystalline LiLuF$_4$:2% Er$^{3+}$,18% Yb$^{3+}$ are compiled in Table 2. Emission spectra for microcrystalline LiLuF$_4$:2% Er$^{3+}$,18% Yb$^{3+}$ have also been recorded at 10 K (Fig. S8, ESI†) as well as from 10 K to 310 K (Fig. S9, ESI†), showing that at low temperatures up to 160 K the $^2H_{11/2} \rightarrow {}^4I_{15/2}$ emission peak is not visible, in agreement to earlier findings.[37]

The value of $\Delta E_2$ can be physically interpreted. At conventionally regarded temperatures ($T < 500$ K), only the thermal coupling between $^2H_{11/2}$ and $^4S_{3/2}$ levels with an energy separation of $\Delta E_1 \sim 750$ cm$^{-1}$ is observed.[33] At higher energies ($\sim 20\,000$ cm$^{-1}$), however, there is also the $^4F_{7/2}$ level of Er$^{3+}$, which is the actually populated level during the energy transfer-based upconversion process with Yb$^{3+}$ (Scheme 1). Although non-radiative relaxation to the lower energetic $^2H_{11/2}$ and $^4S_{3/2}$ levels is the dominant process at lower temperatures, at sufficiently high temperatures, also thermal coupling between the $^4S_{3/2}$ and $^4F_{7/2}$ level with an energy gap of around $\Delta E_2 \sim 1600$ cm$^{-1}$ is expected. The $^4F_{7/2} \rightarrow {}^4I_{15/2}$ emission is usually located around 480–510 nm, which partially overlaps with the $^2H_{11/2} \rightarrow {}^4I_{15/2}$ emission peak,[38] which induces observation of a double Boltzmann behavior of the thermometric ratio $\Delta$ (see also ESI†). In the LiLuF$_4$ material, its presence can be distinctly observed at elevated temperatures (Fig. S10, ESI†). Although the overlap between the emissions is not directly evident from the spectra in the microcrystalline samples, such a spectral overlap of the $^2H_{11/2}$- and the $^4F_{7/2}$-related emission is evident from the evolving shoulder of the emission peaks at around 505–515 nm (see Fig. S10, ESI†). Future experiments in other microcrystalline host compounds are necessary to investigate the role of the $^4F_{7/2}$ level in the Boltzmann equilibrium at temperatures above

Table 2   Table compiling the $\Delta E$ and $R^2$ values obtained from different fitting approaches to the thermometric data of LiLuF$_4$:2% Er$^{3+}$,18% Yb$^{3+}$@LiLuF$_4$@SiO$_2$ nanocrystals and LiLuF$_4$:2% Er$^{3+}$,18% Yb$^{3+}$ microcrystals

| Material | Monoexponential function (eqn (1)) | Two monoexponential functions (divided at 567 K) | Biexponential function (eqn (4)) |
|---|---|---|---|
| LiLuF$_4$:2% Er$^{3+}$,18% Yb$^{3+}$@ LiLuF$_4$@SiO$_2$ nanocrystals | Peak maxima: $\Delta E = 777$ cm$^{-1}$, $R^2 = 0.992$ Area under peaks: $\Delta E = 760$ cm$^{-1}$, $R^2 = 0.997$ | Peak maxima: $\Delta E_1 = 750$ cm$^{-1}$, $\Delta E_2 = 928$ cm$^{-1}$, $R^2 = 0.999$ Area under peaks: $\Delta E_1 = 765$ cm$^{-1}$, $\Delta E_2 = 840$ cm$^{-1}$, $R^2 = 0.999$ | Peak maxima: $\Delta E_1 = (560 \pm 159)$ cm$^{-1}$, $\Delta E_2 = (1390 \pm 364)$ cm$^{-1}$, $R^2 = 0.999$ Area under peaks: $\Delta E_1 = (708 \pm 179)$ cm$^{-1}$, $\Delta E_2 = (1583 \pm 204)$ cm$^{-1}$, $R^2 = 0.999$ |
| LiLuF$_4$:2% Er$^{3+}$,18% Yb$^{3+}$ microcrystals | Peak maxima: $\Delta E = 803$ cm$^{-1}$, $R^2 = 0.991$ Area under peaks: $\Delta E = 742$ cm$^{-1}$, $R^2 = 0.998$ | Peak maxima: $\Delta E_1 = 770$ cm$^{-1}$, $\Delta E_2 = 983$ cm$^{-1}$, $R^2 = 0.999$ Area under peaks: $\Delta E_1 = 730$ cm$^{-1}$, $\Delta E_2 = 817$ cm$^{-1}$, $R^2 = 0.999$ | Peak maxima: $\Delta E_1 = (664 \pm 69)$ cm$^{-1}$, $\Delta E_2 = (1838 \pm 426)$ cm$^{-1}$, $R^2 = 0.999$ Area under peaks: $\Delta E_1 = (673 \pm 179)$ cm$^{-1}$, $\Delta E_2 = (1611 \pm 354)$ cm$^{-1}$, $R^2 = 0.999$ |
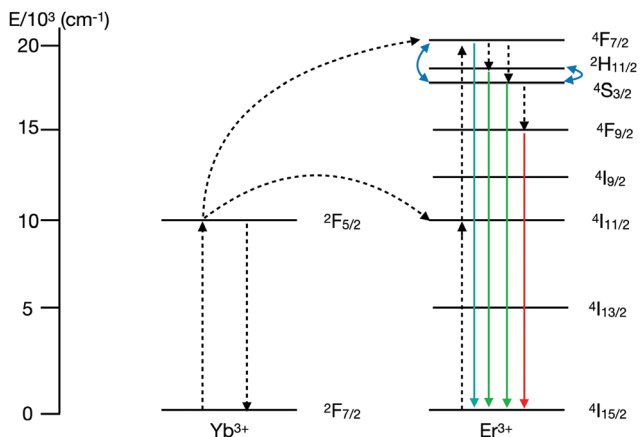
**Scheme 1** Scheme illustrating the participating energy levels of $Yb^{3+}$ and $Er^{3+}$ in the energy transfer–based upconversion mechanism. Thermometry with $Er^{3+}$ results from thermal coupling of the closely spaced $^2H_{11/2}$ and $^4S_{3/2}$ levels, as well as thermalization with the higher energetic $^4F_{7/2}$ level at high temperatures.

500 K is needed to verify whether this is a generally observable behavior of the green LIR of $Er^{3+}$ in inorganic host compounds that can be fitted with the three levels leading to eqn (4). Qualitatively, the observation of a second component in a Boltzmann-type plot of the luminescence intensity ratio $\Delta$ has been previously observed in nanocrystalline $\beta$-$NaYF_4$:$Er^{3+}$,$Yb^{3+}$ and $Y_2O_3$:$Er^{3+}$, $Yb^{3+}$ at high temperatures ($T \gtrsim 550$ K), which indicates that this behavior is common for $Er^{3+}$ at elevated temperatures.[7,14] In what follows, we will give a physical justification for the observed onset temperature for deviation of two-level Boltzmann behavior and also estimate this onset temperature by means of the physically underlying mechanism of phonon absorption.

At higher temperatures, the presence of the $^4F_{7/2}$ excited level cannot be neglected anymore and the thermometric performance of $Er^{3+}$ is understood by considering the ion as a system with three thermally coupled excited levels ($^4F_{7/2}$, $^2H_{11/2}$ and $^4S_{3/2}$). It has already been shown that such an approach with more than two excited levels allows to retain a high relative sensitivity at higher temperatures based on the larger energy gap.[38,39] However, it is also important to realize that this strategy is only useful if there is appreciable luminescence intensity stemming from the radiative transition from the higher excited level ($^4F_{7/2}$). Otherwise, the temperature uncertainty increases despite high relative sensitivity due to the connected low luminescence intensity from the energetically highest of the three excited levels. As recent theoretical considerations have shown,[40] it is possible to accurately estimate the onset temperature above which phonon absorption and thus, thermalization between two excited levels takes place. It is given by eqn (5),

$$T_{\text{on}} \approx 0.2227 \frac{\Delta E_2}{k_B} \qquad (5)$$

With an energy gap of $\Delta E_2 \sim 1600$ cm$^{-1}$ between the $^4S_{3/2}$ and $^4F_{7/2}$ level, an estimated onset temperature of 513 K follows, in very good agreement to the observed temperature

above which a second Boltzmann equilibrium due to thermalization between the $^4F_{7/2}$ and $^4S_{3/2}$ level becomes observable (see *e.g.* Fig. 7e or Table 2). To the best of our knowledge, this is the first time that this mechanism is accounted for in detail. In order to show the possible use of the $LiLuF_4$:2% $Er^{3+}$,18% $Yb^{3+}$@$LiLuF_4$@$SiO_2$ nanoparticles in real high temperature systems repeatability tests (thermal cycling) have been performed, proving they can be heated and cooled down without change in thermometric parameters (Fig. S11, ESI†). Besides the predicted onset of Boltzmann thermalization between the $^4F_{7/2}$ and $^4S_{3/2}$ level, it is also possible to assess its optimum range for temperature measurements. Given the energy gap of $\Delta E_2 \sim 1600$ cm$^{-1}$, recently derived optimization principles for Boltzmann thermometry indicated that the optimum temperature range is[40]

$$T_{\text{opt}} \in \left[ \frac{\Delta E_2}{(2 + \sqrt{2})k_B}, \frac{\Delta E_2}{2k_B} \right] \qquad (6)$$

which affords $T_{\text{opt}} \in [675$ K, $1150$ K$]$, *i.e.* temperature measurements with the $^4F_{7/2}$–$^4S_{3/2}$ energy gap are thermodynamically favored in that given temperature range. Comparingly, the respective advisable temperature range for thermometry with the $^2H_{11/2}$–$^4S_{3/2}$ energy gap of $\sim 750$ cm$^{-1}$ is between 315 K and 540 K. As evident from Fig. 7 and 8, a clear deviation from the single Boltzmann behavior is observed above exactly that predicted range. It is noteworthy that in the reported literature example of nanocrystalline $Y_2O_3$:$Er^{3+}$,$Yb^{3+}$, the energy gap between the barycenters of the $^4F_{7/2}$ and $^4S_{3/2}$ level is higher. For a higher energy gap of 1800 cm$^{-1}$ (possibly even higher), the minimum optimum temperature increases to around 760 K and higher, also in very good agreement with the working ranges of $Er^{3+}$ in different host lattices reported by Geitenbeek *et al.*[7,41,42] Overall, the transition from the $^2H_{11/2}$ – $^4S_{3/2}$ to the $^4F_{7/2}$ – $^4S_{3/2}$ energy gap, causes the relative sensitivity $S_r$ at higher temperatures to be roughly doubled and yet the luminescence intensity ratio is retained at a sufficiently high value to be measured with appreciable precision.

As mentioned earlier in the paper, both the cube-shaped and diamond-shaped nanoparticles showed a peculiar enhancement of the emission intensities of the 525 nm and 550 nm peaks with temperature increase. To further study this, we have recorded the luminescence decay curves of various emission lines for $LiLuF_4$:2% $Er^{3+}$,18% $Yb^{3+}$@$LiLuF_4$ cubic nanoparticles with six shells. This was done by exciting the dried nanoparticle sample at 980 nm with a pulsed excitation source (optical parametric oscillator, OPO). Fig. 9 shows that the decay times observed for the $^2H_{11/2} \rightarrow {}^4I_{15/2}$, $^4S_{3/2} \rightarrow {}^4I_{15/2}$, and $^4F_{9/2} \rightarrow {}^4I_{15/2}$ emissions increase with temperature, consistent with observed increase in emission intensity. Upon raising the temperature from 303 K to 523 K, the average lifetime increased from 270 μs to 825 μs for the $^2H_{11/2} \rightarrow {}^4I_{15/2}$ transition, 300 μs to 678 μs (725 μs for 500 K) for the $^4S_{3/2} \rightarrow {}^4I_{15/2}$ transition and 378 μs to 960 μs for the $^4F_{9/2} \rightarrow {}^4I_{15/2}$ transition. For emission from the thermally coupled $^2H_{11/2}$ and $^4S_{3/2}$ levels identical luminescence lifetimes are expected. The observed differences reflect uncertainty in effective emission lifetimes deduced from non-exponential decay
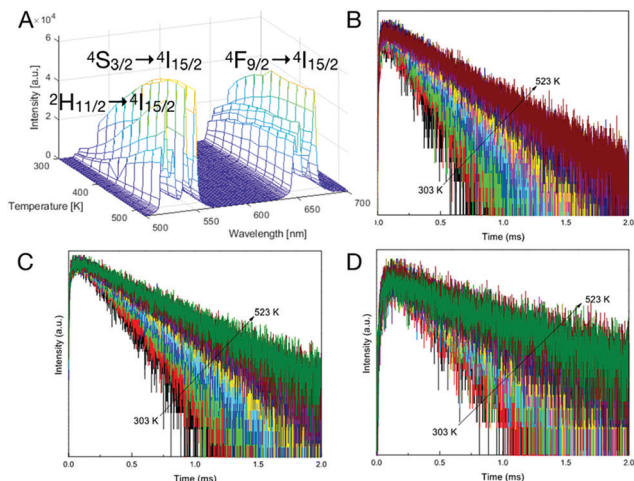
This journal is © The Royal Society of Chemistry 2021

*J. Mater. Chem. C*, 2021, **9**, 3589–3600 | **3597**

Fig. 9  (A) Emission map recorded between 303 K and 523 K for LiLuF$_4$:2% Er$^{3+}$,18% Yb$^{3+}$@LiLuF$_4$ core−shell cubic nanocrystals (six shells) to visualize the $^2H_{11/2} \rightarrow {}^4I_{15/2}$, $^4S_{3/2} \rightarrow {}^4I_{15/2}$, and $^4F_{9/2} \rightarrow {}^4I_{15/2}$ transitions. Luminescence decay curves at varying temperatures were recorded monitoring the $^2H_{11/2} \rightarrow {}^4I_{15/2}$ (B), $^4S_{3/2} \rightarrow {}^4I_{15/2}$ (C) and $^4F_{9/2} \rightarrow {}^4I_{15/2}$ (D) emission, respectively.



Fig. 10  STEM-EDX images for LiLuF$_4$:2% Er$^{3+}$,18% Yb$^{3+}$ core-only cubic nanocrystals. The following elements were mapped: Lu (B), F (C), Yb (D) and Er (E).

curves with a relatively high noise level. It is interesting to observe a lengthening of emission lifetime with temperature as usually decay times decrease with increasing temperature due to the thermally induced increase of the non-radiative decay rates (thermal quenching). The increase in decay time indicates that a non-radiative decay pathway becomes less effective at higher temperatures, which also explains the parallel observation of increased emission intensity at higher temperatures. Removal of water molecules from the surface of nanoparticles could be the cause of such an enhancement in luminescence intensity as demonstrated previously.[36] However, the phenomenon was even more pronounced in the core−shell structures, which is counterintuitive if the previous argument is the underlying reason. In order to gain additional insight into the mechanism for an increase in the measured emission lifetime we have performed thermal cycling tests on the LiLuF$_4$:2% Er$^{3+}$,18% Yb$^{3+}$ (core only) and LiLuF$_4$:2% Er$^{3+}$,18% Yb$^{3+}$@LiLuF$_4$ (6 shells) both in air and N$_2$ atmosphere (by continuously flushing the sample chamber before and during the measurements) (Fig. S12–S15, ESI†).[43] Under N$_2$ atmosphere, after an initial heating step to remove surface adsorbed water molecules, no enhanced luminescence at elevated temperature could be observed in both the core-only and core−shell systems, in agreement to earlier findings.[43] This suggests that removal of water molecules from the surface of the nanocrystals at higher temperatures causes the reduced quenching of Er$^{3+}$. This effect is expected to be less pronounced in the presence of an inert shell around the core particles, which is however not observed. A possible explanation is that the 'inert' shell in fact contains Er$^{3+}$ and Yb$^{3+}$ dopants due to diffusion or another mechanism for dopant incorporation in the shell during shell growth from Li$^+$, Lu$^{3+}$ and F$^-$ precursors. We thus employed STEM-EDX to investigate the core-only and core−shell systems. In the core-only cuboidal particles, the elements F, Lu, Yb and Er are evenly distributed at the surface of the nanoparticles (Fig. 10). The formation of a shell around the core
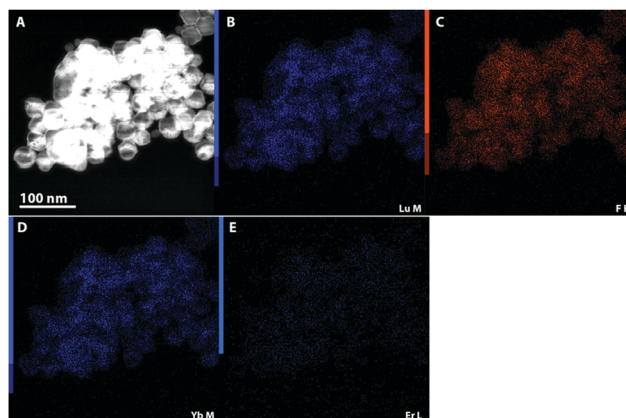
particles was unambiguously proven by the increase in particle size (Fig S16, ESI†). On the other hand, as shown in Fig. 11 (and Fig. S17, ESI†), STEM-EDX analysis indicated that also in the core–shell nanocrystal structures, the elements F, Lu, Yb and Er were distributed all over the particle, including the surface layer, with even more optically active lanthanide dopants (Er and Yb) aggregated within in the shell. The explanation for this aggregation of dopant ions in the shell is not clear at the current stage. Previously, this kind of self-purification has also been observed in quantum dots.[36] Although it should be pointed out that in semiconductors the dopant is chemically very different and there is a driving force for expelling the dopant. However, for lanthanides (especially in the case of used here Lu$^{3+}$, Er$^{3+}$, and Yb$^{3+}$) the sizes are very similar and based on the similar chemical properties of Ln$^{3+}$ ions this type of phenomenon is not expected. Another reason could have been the prolonged high temperature used in the synthesis of the core–shell nanoparticles, which can cause ion migration to the shell (edges) of the nanoparticles. However, we have excluded this factor by prolonging the reaction time of the core-only LiLuF$_4$:2% Er$^{3+}$,18% Yb$^{3+}$ nanocrystals to several hours.
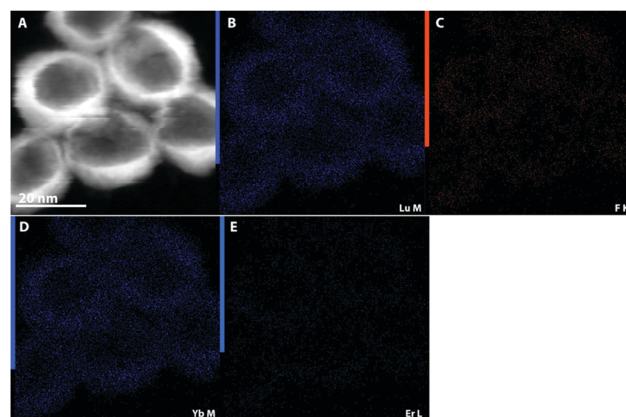


Fig. 11  STEM-EDX images for LiLuF$_4$:2% Er$^{3+}$,18% Yb$^{3+}$@LiLuF$_4$ core−shell cubic nanocrystals (six shells). The following elements were mapped: Lu (B), F (C), Yb (D) and Er (E).

No ion migration to the edges of the particles was observed (Fig. S19 and S20, ESI†). As an overall conclusion, both temperature-dependent luminescence experiments and STEM-EDX analysis clearly prove that the anticipated undoped shells of the nanocrystals actually do contain luminescent dopants. Although an increase in the luminescence intensity is observed in the core–shell particles, this is not attributed to the growth of an inert shell but rather to simply the particle growth as well as the higher degree of crystallinity (less defects) of the core–shell particles compared to the core-only particles. This finding indicates that the underlying mechanism of improved lumines-cence properties upon shelling of nanocrystals by means of a thermal decomposition with trifluoroacetate precursors should be considered with great care and control experiments are needed to investigate the presence of optically active dopants in the shell. At this point we have not investigated if the same issues occur in other core–shell synthesis, *e.g.* in the co-precipitation technique.[44] It is also always valuable to compare the designed nanocrystals with micro-sized crystals of the same material.[45]

## 4. Conclusion

We report the synthesis and characterization of upconverting $LiLuF_4$:2% $Er^{3+}$,18% $Yb^{3+}$ nanocrystals with three different morphologies. Additionally the impact of surrounding shells on the luminescence thermometry properties of the doped $Er^{3+}$ ions was studied. The cubic and diamond-shaped $LiLuF_4$:2% $Er^{3+}$,18% $Yb^{3+}$ nanocrystals as synthesized by a hydrothermal decomposition route from trifluoroacetic acid precursors showed the highest emission intensities and best thermometric performance. Undoped shells were grown around these nano-particles to improve their thermometric behavior over a wide temperature range. It could be demonstrated by means of STEM-EDX studies that the Er- and Yb-dopant ions can be found in various places of the nanocrystals including the undoped shells, consistent with conclusions from temperature dependent luminescence measurements, which showed an impact of luminescence quenching by surface water molecules for both core-only and core–shell nanocrystals. This puts doubts on the hypothesis generally assumed valid that an undoped shell protects the luminescent centers in the core from surface quenching and emphasizes the importance of control experiments to probe the actual dopant distribution in core–shell nanostructures. We also show that coating of the nanoparticles with a silica layer extends the operating range to temperatures above 800 K thus enabling high temperature thermometry. At temperatures around room temperature thermal coupling between the $^{2}H_{11/2}$ and $^{4}S_{3/2}$ energy levels of $Er^{3+}$ is widely used and advisable for Boltzmann-based luminescence thermometry. Here we show that for temperatures above $\sim 550$ K, thermal coupling between the $^{4}S_{3/2}$ and the higher energetic $^{4}F_{7/2}$ level starts to become active. For the first time, we give a combined experimental and theoretical account on this observation and provide thermodynamically motivated quantitative guidelines for thermometry with the $^{4}F_{7/2}$–$^{4}S_{3/2}$

energy gap of $Er^{3+}$ giving rise to higher relative sensitivity at high temperatures.

## Conflicts of interest

There are no conflicts to declare.

## Acknowledgements

## References

1 D. Jaque and F. Vetrone, *Nanoscale*, 2012, **4**, 4301.
2 C. D. S. Brites, P. P. Lima, N. J. O. Silva, A. Millan, V. S. Amaral, F. Palacio and L. D. Carlos, *Nanoscale*, 2012, **4**, 4799.
3 X.-d. Wang, O. S. Wolfbeis and R. J. Meier, *Chem. Soc. Rev.*, 2013, **42**, 7834.
4 Y. Cui, F. Zhu, B. Chen and G. Qian, *Chem. Commun.*, 2015, **51**, 7420.
5 M. Dramicanin, *Luminescence Thermometry, Methods, Materials and Applications*, Woodhead Publishing, 1st edn, 2018.
6 R. G. Geitenbeek, A.-E. Niewelink, T. S. Jacobs, B. B. V. Salzmann, J. Goetze, A. Meijerink and B. M. Weckhuysen, *ACS Catal.*, 2018, **8**, 2397.
7 R. G. Geitenbeek, B. B. V. Salzmann, A.-E. Niewelink, A. Meijerink and B. M. Weckhuysen, *Chem. Eng. Sci.*, 2019, **198**, 235.
8 L. T. Yeh, *J. Electron. Packag.*, 1995, **117**, 333.
9 J. Jaramillo-Fernandez, E. Chavez-Angel and C. M. Sotomayor-Torres, *Appl. Therm. Eng*, 2018, **130**, 1175.
10 C. D. S. Brites, S. Balabhadra and L. D. Carlos, *Adv. Opt. Mater.*, 2018, 1801239.
11 F. Vetrone, R. Naccache, A. Zamarron, A. Juarranz de la Fuente, F. Sanz-Rodriguez, L. M. Maestro, E. M. Rodriguez, D. Jaque, J. G. Sole and J. A. Capobianco, *ACS Nano*, 2010, **4**, 3254.
12 E. C. Ximendes, U. Rocha, T. O. Sales, N. Fernandez, F. Sanz-Rodriguez, I. R. Martin, C. Jacinto and D. Jaque, *Adv. Funct. Mater.*, 2017, 1702249.
13 K. Elzbieciak and L. Marciniak, *Front. Chem.*, 2018, **6**, 424.
14 R. G. Geitenbeek, P. T. Prins, W. Albrecht, A. van Blaaderen, B. M. Weckhuysen and A. Meijerink, *J. Phys. Chem. C*, 2017, **121**, 3503.
15 M. N. Getz, O. Nilsen and P.-A. Hansen, *Sci. Rep.*, 2019, **9**, 10247.
16 R. G. Geitenbeek, H. W. de Wijn and A. Meijerink, *Phys. Rev. Appl.*, 2018, **10**, 064006.
17 J.-C. G. Bünzli and C. Piguet, *Chem. Soc. Rev.*, 2005, **34**, 1048.

This journal is © The Royal Society of Chemistry 2021

*J. Mater. Chem. C*, 2021, **9**, 3589–3600 | **3599**

18 J.-C. G. Bünzli, *Acc. Chem. Res.*, 2006, **39**, 53.

19 Y. Cheng, Y. Gao, H. Lin, F. Huang and Y. Wang, *J. Mater. Chem. C*, 2018, **6**, 7462.

20 Y. Zhu, S. Zhao, B. Zhou, H. Zhu and Y. Wang, *J. Phys. Chem. C*, 2017, **121**, 18909.

21 J. Liu, H. Rijckaert, M. Zeng, K. Haustraete, B. Laforce, L. Vincze, I. Van Driessche, A. M. Kaczmarek and R. Van Deun, *Adv. Funct. Mater.*, 2018, **28**, 1707365.

22 B. Zhou, B. Xu, H. He, Z. Gu, B. Tang, Y. Ma and T. Zhai, *Nanoscale*, 2018, **10**, 2834.

23 J.-C. Boyer, F. Vetrone, L. A. Cuccia and J. A. Capobianco, *J. Am. Chem. Soc.*, 2006, **128**, 7444.

24 A. Skripka, A. Morivil, M. Matulionyte, T. Cheng and F. Vetrone, *Nanoscale*, 2019, **11**, 11322.

25 P. Huang, W. Zheng, D. Tu, X. Shang, M. Zhang, R. Li, J. Xu, Y. Liu and X. Chen, *Adv. Sci.*, 2019, **6**, 1802282.

26 P. Huang, W. Zheng, S. Zhou, D. Tu, Z. Chen, H. Zhu, R. Li, E. Ma, M. Huang and X. Chen, *Angew. Chem., Int. Ed.*, 2014, **53**, 1252.

27 L. Cai, Y. Huang, P. Sun, W. Zheng, S. Zhou, P. Huang, J. Wei, D. Tu, X. Chen and Z. Liang, *Nanoscale*, 2020, **12**, 6729.

28 A. R. N. Bastos, C. D. S. Brites, P. A. Rojas-Gutierrez, C. DeWolf, R. A. S. Ferreira, J. A. Capobianco and L. D. Carlos, *Adv. Funct. Mater.*, 2019, **7**, 1905474.

29 A. V. Goryunov, A. I. Popov, N. M. Khajdukov and P. P. Fedorov, *Mater. Res. Bull.*, 1992, **27**, 213.

30 A. Grzechnik, K. Friese, V. Dmitriev, H.-P. Weber, J.-Y. Gesland and W. A. Crichton, *J. Phys.: Condens. Matter*, 2005, **17**, 163.

31 J. Liu, R. Van Deun and A. M. Kaczmarek, *Nanomaterials*, 2019, **9**, 646.

32 C. D. S. Brites, A. Millan and L. D. Carlos, *Handbook on the Physics and Chemistry of Rare Earths*, 2016, **49**, 339.

33 W. T. Carnall, P. R. Fields and K. Rajnak, *J. Chem. Phys.*, 1968, **49**, 4424.

34 A. M. Kaczmarek, M. K. Kaczmarek and R. Van Deun, *Nanoscale*, 2019, **11**, 833.

35 A. M. Kaczmarek, Y.-Y. Liu, M. K. Kaczmarek, H. Liu, F. Artizzu, L. D. Carlos and P. Van Der Voort, *Angew. Chem., Int. Ed.*, 2020, **59**, 1932.

36 G. M. Dalpian and J. R. Chelikowsky, *Phys. Rev. Lett.*, 2006, **96**, 226802.

37 J. A. Capobianco, P. Kabro, F. S. Ermeneux, R. Moncorgé, M. Bettinelli and E. Cavalli, *Chem. Phys.*, 1997, **214**, 329.

38 A. Ciric, J. Aleksic, T. Barudzija, Z. Antic, V. Dordevic, M. Medic, J. Perisa, I. Zekovic, M. Mitric and M. D. Dramicanin, *Nanomaterials*, 2020, **10**, 627.

39 L. Li, F. Qin, Y. Zhou, Y. Zheng, J. Miao and Z. Zhang, *Sens. Actuators, A*, 2020, **304**, 111864.

40 M. Suta and A. Meijerink, *Adv. Theory Simul.*, 2020, **3**, 2000176.

41 J. I. Eldridge, *J. Lumin.*, 2019, **214**, 116535.

42 W. F. Krupke, *Phys. Rev.*, 1966, **145**, 325.

43 Z. Wang, J. Christiansen, D. Wezendonk, X. Xie, M. A. van Huis and A. Meijerink, *Nanoscale*, 2019, **11**, 12188.

44 D. Chen, M. Xu and P. Huang, *Sens. Actuators, B*, 2016, **231**, 576.

45 H. Sua, X. Zhao, Z. Zhang, T. Li, E. M. Goldys and C. Guo, *Chem. Eng. J.*, 2017, **313**(1), 65.

**3600** | *J. Mater. Chem. C*, 2021, **9**, 3589–3600

This journal is © The Royal Society of Chemistry 2021